

Melt-electrowriting of 3D anatomically relevant scaffolds to recreate a pancreatic acinar unit in vitro

*Original*

Melt-electrowriting of 3D anatomically relevant scaffolds to recreate a pancreatic acinar unit in vitro / Sgarminato, Viola; Licciardello, Michela; Ciardelli, Gianluca; Tonda-Turo, Chiara. - In: INTERNATIONAL JOURNAL OF BIOPRINTING. - ISSN 2424-8002. - 10:2(2024), pp. 413-430. [10.36922/ijb.1975]

*Availability:*

This version is available at: 11583/2988183 since: 2024-04-29T15:08:48Z

*Publisher:*

AccScience Publishing

*Published*

DOI:10.36922/ijb.1975

*Terms of use:*

This article is made available under terms and conditions as specified in the corresponding bibliographic description in the repository

*Publisher copyright*

(Article begins on next page)

## RESEARCH ARTICLE

# Melt-electrowriting of 3D anatomically relevant scaffolds to recreate a pancreatic acinar unit *in vitro*

**Viola Sgarminato<sup>1,2,3</sup>, Michela Licciardello<sup>1,2,3</sup>, Gianluca Ciardelli<sup>1,2,3,4†</sup>, and Chiara Tonda-Turo<sup>1,2,3,\*†</sup>**

<sup>1</sup>Department of Mechanical and Aerospace Engineering, Politecnico di Torino, Turin, Italy

<sup>2</sup>POLITO BIOMedLAB, Politecnico di Torino, Turin, Italy

<sup>3</sup>Interuniversity Center for the Promotion of the 3Rs Principles in Teaching and Research, Pisa, Italy

<sup>4</sup>CNR-IPCF, National Research Council-Institute for Chemical and Physical Processes, Pisa, Italy

(This article belongs to the *Special Issue: 3D Bioprinting for Tumor Modeling*)

## Abstract

Melt-electrowriting (MEW) belongs to the group of advanced additive manufacturing techniques and consists of computer-aided design (CAD)-assisted polymer extrusion combined with a high-voltage supply to achieve deposition of polymeric fibers with diameters in the micrometric range (1 to 20  $\mu\text{m}$ ) similar to the size of natural extracellular matrix fibers. In this work, we exploit MEW to design and fabricate a three-dimensional (3D) model that resembles the morphology of the exocrine pancreatic functional unit without the need of supports, mandrels, or sacrificial materials. Optimized process parameters resulted in a MEW scaffold having regular fibers (19  $\pm$  5  $\mu\text{m}$  size) and an acinar cavity showing high shape fidelity. Then, human foreskin fibroblasts (HFF1) and human pancreatic ductal epithelial cells (HPDE), wild-type HPDE, and HPDE overexpressing *KRAS* oncogene were allowed to colonize the entire 3D structure and the acinar cavity. Thus, a physiologically relevant 3D model was created *in vitro* after 24 days using a co-culture protocol (14 days of HFF1 alone plus 10 days of HPDE and HFF1 co-culture). The effect of cell crosstalk within the MEW scaffolds was also assessed by monitoring HFF1 secretion of interleukin (IL)-6, a pro-inflammatory cytokine responsible for the inflammatory cascade occurring in pancreatic cancer. High levels of IL-6 were detected only when fibroblasts were co-cultured with the HPDE overexpressing *KRAS*. These findings confirmed that the MEW 3D *in vitro* model is able to recreate the characteristic hallmark of the pathological condition where cancer oncogenes mediate fibroblast activities.

**Keywords:** Melt-electrowriting; Exocrine pancreas; *In vitro* models; 3D scaffolds; Pancreatic ductal adenocarcinoma

†These authors contributed equally to this work.

**\*Corresponding author:**

Chiara Tonda-Turo  
 (chiara.tondaturo@polito.it)

**Citation:** Sgarminato V, Licciardello M, Ciardelli G, Tonda-Turo C.

Melt-electrowriting of 3D anatomically relevant scaffolds to recreate a pancreatic acinar unit *in vitro*. *Int J Bioprint*. 2024;10(2):1975.  
 doi: 10.36922/ijb.1975

**Received:** October 6, 2023

**Accepted:** November 17, 2023

**Published Online:** February 23, 2024

**Copyright:** © 2024 Author(s).

This is an Open Access article distributed under the terms of the Creative Commons Attribution License, permitting distribution, and reproduction in any medium, provided the original work is properly cited.

**Publisher's Note:** AccScience Publishing remains neutral with regard to jurisdictional claims in published maps and institutional affiliations.

## 1. Introduction

Pancreatic adenomeres secreting the digestive enzymes are the functional units of exocrine pancreas and are the sites where the first lesions of pancreatic ductal adenocarcinoma (PDAC) develop. In pancreas, an adenomere is constituted by acinar and ductal

epithelial cells surrounded by a thin basal lamina, stromal tissue, and pancreatic stellate cells (PSCs).<sup>1,2</sup> The PSCs are stromal cells responsible for the intense desmoplastic reaction occurring during the PDAC development.<sup>3,4</sup> Indeed, in healthy tissue, PSCs are characterized by high expression of both ectodermal and mesenchymal markers and significant amount of retinoids such as vitamin A in lipid droplets.<sup>5</sup>

Under the influence of inflammatory cues and cancer cells-derived factors, PSCs become active and assume a myofibroblast-like phenotype capable of deregulating extracellular matrix (ECM) homeostasis.<sup>6</sup> Typically, activated PSCs surround the cancer cells and communicate with them via different cytokines and factors (i.e., interleukin [IL]-6, IL-1 $\beta$ , and transforming growth factor beta [TGF- $\beta$ ]), through complex autocrine and paracrine signaling pathways.<sup>7-9</sup> Therefore, the interplay between cancer and stromal cells plays a key role in tumor evolution, promoting the pancreatic cancer progression by significantly affecting gene expression patterns, metabolic activities, invasion/metastasis phenomena, and resistance mechanisms.<sup>10</sup> However, the mechanisms implicated in the early stages of PDAC evolution, as well as the complex and dynamic phenomena involved in the crosstalk between cancer epithelial and stromal cells, still remain unclear.<sup>11</sup> This lack of knowledge limits the possibilities of early PDAC diagnosis, thereby resulting in a poor clinical prognosis. Indeed, the number of patients undergoing surgical resection is below 10%, as most of clinical cases have spread metastases at diagnosis.<sup>12,13</sup> Furthermore, the extremely complex bioarchitecture of the pancreatic tumor microenvironment (TME) affects the efficacy of drugs and causes the failure of current therapeutic strategies that are inadequate to treat this extremely aggressive cancer.<sup>12,14</sup> To improve the knowledge of the disease with the ultimate goal of performing early diagnoses and designing effective therapies for enhancing patients' prognosis, functional and reliable *in vitro* models need to be designed and fabricated.<sup>15-20</sup>

For many years, cancer research has been conducted using two-dimensional cell cultures and animal models, which poorly recapitulate the biological complexity of the disease in humans. Recent efforts in creating more representative preclinical *in vitro* models have led to the development of experimental replica of human tissues in a 3D environment or inside a microfluidic chip (organ-on-chip). PDAC-on-chip permits the recapitulation of the physiological crosstalk between different cell phenotypes and the high-throughput analysis,<sup>21</sup> but it is unable to mimic the 3D complex gland morphology of the functional unit of exocrine pancreas. Nevertheless, it remains a challenge to reproduce the microanatomy of the exocrine pancreas (intended as 3D architecture and cellular composition) in

3D biomimetic platforms, which fail to fully recapitulate the native compartmentalized architecture of tumor microenvironment, which is known to affect cell activity and cancer-cell response to drugs.<sup>5,22,23</sup> Specifically, the glandular morphology has been mimicked by using different techniques,<sup>24-27</sup> which however have limitations such as low reproducibility, throughput, and shape fidelity.

The present work focuses on the development of a 3D *in vitro* model that resembles the functional unit of exocrine pancreas through melt-electrowriting (MEW). MEW technology combines principles of conventional electrospinning (solution electrospinning) with melt extrusion-based methods,<sup>28,29</sup> and it can be defined as a contactless 3D printing technique due to the longer distance between needle and print bed. Indeed, like solution electrospinning, a high voltage (HV) is applied between the nozzle and the collector to exert an electrostatic attraction on the molten material, and a so-called Taylor cone forms at the nozzle tip. The electrical field forces the formation of a microscale polymer filament from the Taylor cone, which is deposited into a micrometer fiber on the collector.<sup>28,29</sup> Due to the distance between nozzle and platform and the fiber stretching induced by the electric field, the size of the extruded filament in MEW is about ten times lower than the filament diameter obtained by fused deposition modeling (FDM) where the distance between nozzle and collector is minimal (i.e., a few hundreds of microns),<sup>30</sup> thus resulting in a better resolution of the printed structures.<sup>31</sup> Compared to other extrusion-based techniques, such as 3D bioprinting, MEW allows to achieve better resolutions, in terms of minimum feature width, and higher geometrical accuracy due to the use of thermoplastic polymers instead of cell-laden hydrogels.<sup>32,33</sup>

For these reasons, MEW was adopted in this work to obtain microscale polycaprolactone (PCL) scaffolds mimicking the half structure of the pancreatic acinus (Figure 1a and b) having a resolution and size not achievable with the 3D printing technologies available so far. The use of this synthetic thermoplastic polymer (PCL) has been widely adopted in the fabrication of scaffolds as it is highly processable by electrospinning<sup>34-36</sup> and additive manufacturing,<sup>37-40</sup> and it is recognized to support cell attachment, migration, growth, and long-term cultures. Then, MEW scaffolds were seeded with stromal cells (human fibroblasts) (Figure 1c<sub>i</sub>) and HPDE (both healthy HPDE and HPDE overexpressing *KRAS* oncogene) to develop the 3D models (Figure 1c<sub>ii</sub>) having a biomimetic geometry and cell distribution.

## 2. Materials and methods

### 2.1. Cell culture

Human pancreatic ductal epithelial cells (HPDE)—both wild-type HPDE (HPDE-WT) and HPDE stably expressing

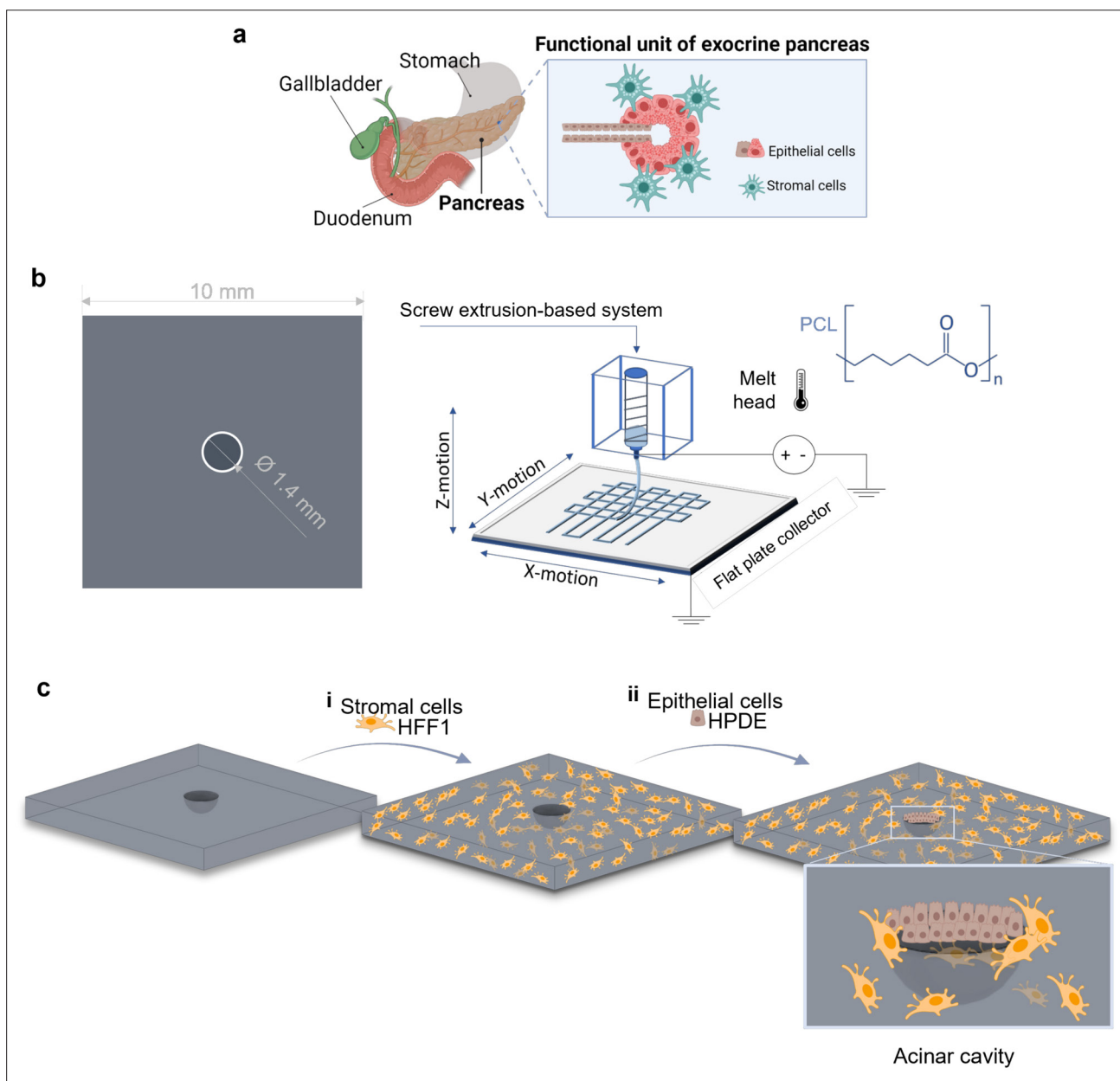


**Figure 1.** 3D layer-by-layer *in vitro* model. (a) Illustration of the functional unit of exocrine pancreas, composed by epithelial cells surrounded by stromal cells. (b) Melt-electrowriting (MEW) was employed: CAD drawings, processing of polycaprolactone (PCL), and production of a microscopic *in vitro* model. (c) The MEW scaffolds were then cellularized by seeding human fibroblasts (i) and epithelial cells (ii). Figure drawn using Biorender.com.

activated *KRAS* (HPDE-*KRAS*)—were kindly provided by Prof. F. Bussolino (Candiolo Cancer Institute-IRCCS-FPO, Candiolo, Italy). The cells were cultured in RPMI-1640 medium (Gibco, Jenks, USA) supplemented with 1% penicillin–streptomycin (Gibco), 1% L-glutamine (Gibco), and 10% fetal bovine serum (FBS; Gibco). Human foreskin fibroblasts (HFF1) cells were obtained from ATCC® and cultured in Dulbecco’s Modified Eagle’s Medium (DMEM) supplemented with 1% penicillin–streptomycin (Gibco),

2% L-glutamine (Gibco), and 15% FBS (Gibco). Cell lines were maintained in a humidified CO<sub>2</sub> incubator at 37°C and 5% CO<sub>2</sub>.

## 2.2. Scaffold design and fabrication by MEW

The 3D MEW models were designed through SolidWorks® CAD software. The CAD models consist of a square-based 3D structure with a central cavity (Figure 1c). The cuboid had a final dimension of 10 mm (length) × 10 mm



(width) × 2.5 mm (thickness), while the central cavity was designed with a diameter of 1.4 mm. CAD models were discretized into triangles, and .stl files were thus generated. Then, the g-codes were obtained using the Ultimaker Cura 4.8.0 software by setting the parameters needed to perform the slicing and later optimized using the Repetier-Host and NC Viewer v1.1.3 software. Specifically, the automated g-codes, generated by the .stl files slicing, were further edited to (i) prevent the needle from passing over the scaffold between one layer and the next, so as to avoid depositing undesired fibers; and (ii) implement an additional extrusion step at the initial phase of the printing process, in order to stabilize the jet. Then, NovaSpider v5 instrument (CIC nanoGUNE) was employed to fabricate PCL (Mw ~ 43,000 Da; 19561-500, Polysciences Inc., Warrington, USA) scaffolds by MEW. To achieve a printed structure with proper filament diameter, pore size, and shape fidelity, several process parameters were tested, by varying their values in the ranges shown in Table 1. Ambient parameters (i.e., chamber temperature and humidity) were set at 27.5°C ± 3°C and 44% ± 2%, respectively. In detail, the humidity was monitored and controlled by an external humidifier (miniClima Humidity Control, miniClima Schönbauer GmbH, Wien, Austria) connected to the NovaSpider apparatus.

### 2.3. Dimensional analyses

The effect of parameters on printed scaffold resolution was evaluated by scanning electron microscopy (SEM; Tescan Vega, Brno-Kohoutovice, Czech Republic) of MEW scaffolds. Before analysis, all the samples were coated with a thin platinum layer. SEM images were then analyzed using ImageJ<sup>41</sup> to quantify the average size of fibers. In detail, two scaffolds per condition were examined, and 40 values for each scaffold were measured.

### 2.4. Seeding of stromal cells in MEW constructs

At first, the MEW constructs were incubated in a solution containing 70% ethanol and 30% water overnight and then

irradiated with ultraviolet light for 1 h (30 min on each side) for sterilization purposes before cell seeding.

Human fibroblasts were seeded in sterile MEW scaffolds placed in a 48-well plate. In particular, HFF1 were seeded on MEW constructs by pipetting 40 µL of a 1.6 × 10<sup>6</sup> cells/mL cell suspension on the top of the scaffolds. The constructs were maintained at 37°C and 5% CO<sub>2</sub> for 1 h before 600 µL of medium was added to each well.

### 2.5. Viability assay

The viability of human fibroblasts (HFF1) cultured in MEW constructs was evaluated through the fluorimetric resazurin reduction method (CellTiter-Blue, G8080, Promega, Milano, Italy) 3, 7, 14, 21, and 28 days after seeding. The assay was carried out according to the manufacturers' protocols. Briefly, culture medium was removed, and constructs were washed with 1× phosphate-buffered saline (PBS; Gibco). A solution of 16% CellTiter-Blue in complete cell culture medium was prepared and added to the constructs. After an incubation period of 3–4 h at 37°C, 100 µL of the medium was pipetted into different wells of a 96-well plate, and fluorescence was measured using a plate reader (Synergy HTX Multi-Mode Reader, BioTek) at 530 nm excitation wavelength and 590 nm emission wavelength. All the obtained data were then exported and elaborated using GraphPad Prism 9.3.1.

### 2.6. Stromal cells distribution within MEW scaffolds: confocal microscopy and scanning electron microscopy analyses

Fluorescence imaging was performed to monitor the distribution of stromal cells (HFF1) seeded within the 3D scaffolds. The constructs were washed once with 1× PBS and fixed with 4% paraformaldehyde (PFA; Sigma Aldrich) for 30 min at room temperature, after 72 h of culture. They were then washed twice with 1× PBS, permeabilized in 0.5% Triton X-100 (Sigma Aldrich) in 1× PBS for 10 min, and incubated with 1% bovine serum albumin (BSA; Invitrogen, Carlsbad, CA, USA) for 30 min to enhance the quality of the staining. The cytoskeletons of fibroblasts in MEW scaffolds were stained with Alexa Fluor™ 488 Phalloidin (A12379, Invitrogen) at 1:60 concentration in a solution of 1× PBS with 1% BSA. Nuclei were stained with DAPI reagent (4',6-diamidino-2-phenylindole, Dihydrochloride; D1306, Invitrogen) at 1:1000 concentration in 1× PBS solution. All samples were then imaged by confocal microscopy (Eclipse Ti2, Nikon, Konan Minato-ku, Japan). The resulting images were post-processed with ImageJ software.

Furthermore, SEM analyses were performed upon dehydration of fixed fibroblasts within the scaffolds to observe both HFF1 cells and the MEW filaments. Samples were dehydrated by soaking them into ethanol/

**Table 1. Process parameters used to fabricate the MEW scaffolds**

Scaffold type	i	ii	iii	iv
Nozzle size (mm)	0.5	0.5	0.5	0.3
Flow (%)	20	40	40	20
Infill line distance (µm)	80	110	110	80
Infill rotate angle (°)	45	45	90	90
Speed (mm/s)	70	60	60	40
Distance (mm)	7	6	6	12
Printing temperature (°C)	130	100	100	90
Voltage (kV)	5	7	5	5

water solutions starting from 30/70 up to 100/0. Before analysis, all the samples were coated with a thin platinum layer.

### 2.7. Epithelization of the cavity

HPDE-KRAS and HPDE-WT cells were detached from the culture flask, counted, and resuspended to a 10  $\mu$ L volume to obtain a  $2.1 \times 10^6$  cells/mL concentration. Then, cells were seeded into the cavity of cellularized MEW scaffold, where HFF1 were allowed to grow for 2 weeks. The co-cultured constructs were placed in a 48-well plate.

The HPDE cells/HFF1 cell ratio was set at 1:3, according to studies demonstrating the relevancy that ratios of 1:1 to 1:3 have *in vivo*.<sup>42-44</sup> Cells were co-cultured in DMEM/F-12 supplemented with 15% FBS (Gibco), 1% penicillin-streptomycin (Gibco), and 2% L-glutamine (Gibco) since previous experiments had proven the efficacy of this culture medium composition in promoting cell viability.<sup>21</sup> The constructs were then fully covered with 600  $\mu$ L of medium after 60 min. The cellularized structures were maintained in a humidified CO<sub>2</sub> incubator at 37°C and 5% CO<sub>2</sub>.

### 2.8. Immunocytochemistry and confocal microscopy

The co-cultured MEW constructs were fixed with 4% paraformaldehyde (PFA; Sigma Aldrich) for 30 min at room temperature, after 3, 7, 10, and 14 days of co-culture. They were then rinsed with PBS twice and kept at 4°C. Each sample was then permeabilized with 0.2% Triton X-100 in PBS for 10 min at room temperature and successively washed 3 times for 5 minutes with PBS + 0.1% Tween 20 (PBST) at room temperature. Then, samples were blocked with 2% BSA in PBST for 60 min and rinsed three times with PBST. The samples were incubated with primary antibodies—alpha-smooth muscle actin recombinant rabbit monoclonal antibody (1:200; 701457 100  $\mu$ g, Invitrogen) and E-cadherin monoclonal antibody (HECD-1; 1:2000; 13-1700, Invitrogen)—in PBST + 1% BSA for 24 h at 4°C. Samples were then rinsed 3 times with PBST at room temperature for 5 min. Then, the samples were incubated with secondary antibodies—Cyanine5-conjugated goat anti-mouse secondary antibody (1:200; A10524, Invitrogen) and Alexa Fluor™ 555-conjugated goat anti-rabbit secondary antibody (1:500; A27017, Invitrogen)—in PBST + 1% BSA for 2 h at room temperature. Samples were rinsed with PBST for 5 min at room temperature thrice. The cytoskeletons of HFF1 and HPDE cells seeded in MEW scaffolds were then stained with Alexa Fluor™ 488 Phalloidin (A12379, Invitrogen) at 1:60 concentration in a solution of 1 $\times$  PBS with 1% BSA. Samples were rinsed with PBS for 5 min at room temperature thrice, before the staining with DAPI (D1306, Invitrogen) in PBS (1:1000) for 5 min at room temperature. They were then washed once with PBS, and

finally mounted on glass coverslips using Fluoromount™ Aqueous Mounting Medium (00-4958-02, Invitrogen) for imaging. All samples were then imaged by confocal microscopy (Eclipse Ti2, Nikon). The resulting images were post-processed and analyzed with ImageJ software. In particular, the fluorescence intensity (mean gray values along the z-axis) corresponding to the E-cadherin signal was analyzed in z-stack acquisitions and plotted to compare the epithelial cell distributions within the cavity of the MEW scaffold at different time points of culture period. The fluorescence intensity values were normalized to the minimum value measured by the software for each sample.

### 2.9. Interleukin-6 cytokines release

The concentration of cytokines was determined in cell supernatants collected, after 2, 3, 10, and 14 days from HPDE cells seeding, from the wells containing the MEW scaffolds co-cultured with HFF1, HFF1 + HPDE-KRAS, and HFF1 + HPDE-WT cells. IL-6 cytokines were quantified with the IL-6 Human ELISA Kit (BMS213-2, Invitrogen). The concentrations were calculated using the standard curve generated by plotting the absorbance values of each standard sample on the ordinate and the human IL-6 standard concentrations on the abscissa.

### 2.10. Statistical analysis

All bar graph data are presented as the mean  $\pm$  standard deviation (SD) from at least three independent experiments per condition or time point. Significance was measured as indicated for each experiment, with two-way or one-way analysis of variance (ANOVA) followed by pairwise comparison with Tukey's multiple comparisons test using GraphPad Prism 9.3.1; \* $p < 0.05$ , \*\* $p < 0.01$ , \*\*\* $p < 0.001$ , \*\*\*\* $p < 0.0001$ .

## 3. Results

### 3.1. Fabrication of acinar structures

The effect of the process parameters on the resulted MEW scaffolds was evaluated qualitatively by observing the print shape fidelity with respect to the CAD design at the macroscopic and microscopic levels, and quantitatively by measuring the diameter of fibers. The SEM images in [Figure 2a](#) show representative images of MEW scaffolds produced by varying the process parameters in the ranges reported in [Table 1](#). Specifically, the structures were obtained with: 0.5 mm (i-iii) and 0.3 mm (iv) nozzle size; 20% (i, iv) and 40% (ii, iii) flow; 80  $\mu$ m (i, iv) and 110  $\mu$ m (ii, iii) infill line distance; 45° (i, ii) and 90° (iii, iv) infill rotate angle; 70 mm/s (i), 60 mm/s (ii, iii), and 40 mm/s (iv) speed; 7 mm (i), 6 mm (ii, iii), and 12 mm (iv) distance; 130°C (i), 100°C (ii, iii), and 90°C (iv) printing temperature; and 5 kV (i, iii, iv) and 7 kV (ii) voltage.

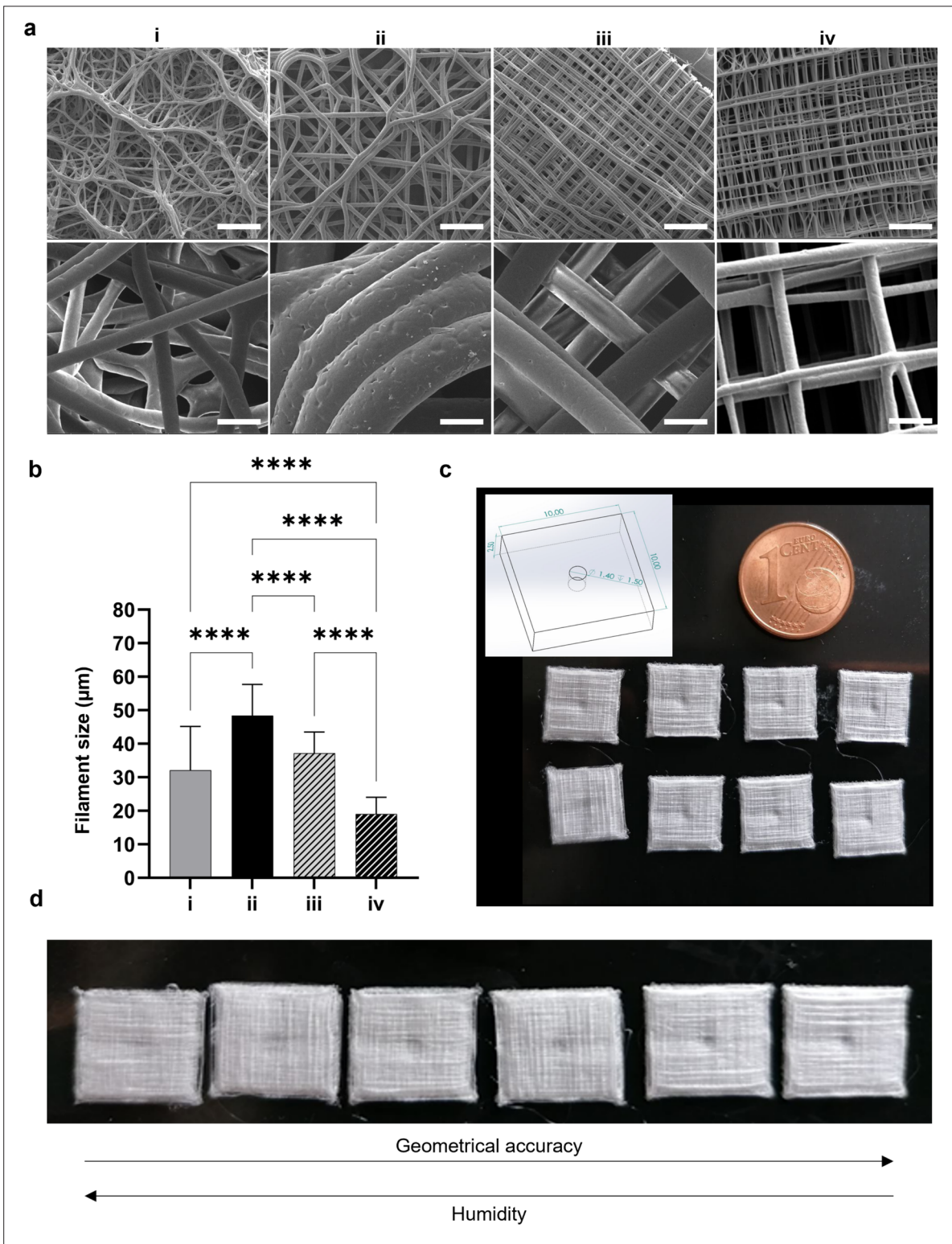


**Figure 2.** Fabrication of acinar structures by melt-electrowriting (MEW). (a) Scanning electron microscopy (SEM) images of scaffolds obtained by setting different process parameters, according to Table 1. Scale bars: 500 µm (first row) and 100 µm (second row). (b) Bar plots reporting the dimensional analysis (filament size) on the different scaffold types ( $n = 2$ ; 40 images per scaffold). Tukey’s multiple comparisons test: \* $p < 0.05$ , \*\* $p < 0.01$ , \*\*\* $p < 0.001$ , \*\*\*\* $p < 0.0001$ . (c) CAD drawing and photographs of the printed structures corresponding to scaffold type iv. (d) Photographs showing the relationship between geometrical accuracy and humidity, which varies between 44% and 54%.



The differences in terms of precision in filament deposition, pore interconnectivity, and fiber size in MEW scaffolds were observed. In general, the constructs obtained with the highest printing temperature (130°C) had randomly deposited fibers (Figure 2a<sub>i</sub>), while the pores of scaffolds produced with an infill deposition angle of 45° were poorly interconnected (Figure 2a<sub>ii</sub>). Decreasing the flow and the nozzle diameter and increasing the distance between needle and platform improve the accuracy of filament deposition and the structure resolution as the filament size also decreases (Figure 2a<sub>iii-iv</sub> and b). The scaffolds with the best resolution and pore interconnectivity (scaffold type iv) were chosen as optimal constructs for cell culture. Several replicas as shown in Figure 2c show high reproducibility of the manufacturing process.

Geometrical accuracy and shape fidelity were found to be affected by ambient parameters rather than the process parameters as shown in Figure 2d. Specifically, by decreasing the humidity from 54% to 44%, the geometry accuracy of printed constructs visibly improves.

### 3.2. Viability and distribution of stromal cells in MEW model

Figure 3a shows the viability of stromal cells, measured by a fluorometric/colorimetric assay, in which the metabolic capacity of live cells is quantified. The results demonstrate the ability of MEW constructs in supporting the growth of human fibroblasts for a period of up to 28 days. In particular, a statistically significant ( $p < 0.0001$ ) increment in cell viability occurred from 3 days, 7 days, and 14 days to 28 days. On the contrary, the increment from 21 days to 28 days was minimal.

The distribution of cells inside the 3D scaffolds was evaluated by fluorescence microscopy and SEM analyses on the cellularized structures. Representative confocal and SEM images of MEW scaffolds seeded with HFF1 are depicted in Figures 3b and 4. An increment in stromal cells proliferation within the 3D MEW structures can be qualitatively observed from 14 days to 21 days and 28 days (Figure 4). Starting from 3 weeks of culture, the formation of a stromal matrix occurred, and the developed new tissue covered much of the scaffold surface after 28 days in culture. Indeed, the presence of granular corpuscles on the fibers at 21 days and 28 days after seeding could be ascribed to the ECM deposited by HFF1. The fiber dimension comparable to the cell size allowed an optimal colonization by fibroblasts that were able to adhere to different fibers, creating bridges across the pores, and to grow with support by the polymeric grid, indicating that a biomimetic process is in progress.

### 3.3. Crosstalk between epithelial and stromal cells in MEW model

The ability of the developed MEW model in reproducing the natural compartmentalization typical of the exocrine pancreatic microenvironment was analyzed (Figure 5). In particular, the interactions between epithelial and stromal cells were evaluated by quantifying the release of pro-inflammatory cues through the ELISA test and by observing the cell distribution (Figure 5a). Interleukin-6 release was measured in serum collected by MEW models seeded with HFF1 (monoculture), HFF1 + HPDE-KRAS cells or HFF1 + HPDE-WT cells at different time points of the culture period. As shown in Figure 5b, the level of IL-6 was higher for fibroblasts co-cultured with HPDE-KRAS cells at 2 days and 3 days, as compared with other conditions (HFF1 and HFF1 + HPDE-WT). This finding points to the augmented inflammation caused by the presence of HPDE-KRAS cells in co-culture with stromal cells. However, at later time points (10 days and 14 days), the IL-6 release decreased, suggesting that inflammation mediated by pro-inflammatory cytokines such as IL-6 mainly occurred in the initial phase of tumor–stroma crosstalk. Figure 5c shows the plots relative to E-cadherin signal from epithelial cells measured in the z-stack acquisitions from the top of the model to the bottom of the cavity (Figure 5d). The z-stack videos (Videos S1–S3 in Supplementary File) and the confocal images in Figure 6 demonstrate the presence of HPDE-KRAS cells predominantly inside the cavity of the MEW scaffolds, thus confirming the success of the seeding procedure. The epithelial cells remained collimated in the biomimetic cavity for 10 days, while they were also visible in the portion around the cavity 14 days after seeding. Indeed, the plots of the signal corresponding to 7 and 10 days after seeding are characterized by a peak of fluorescence intensity in correspondence to the cavity's bottom ( $z \approx 700 \mu\text{m}$ ), while the fluorescence intensity of epithelial cells co-cultured for 14 days with HFF1 resulted highest for the focal planes proximal to the upper surface of the model ( $z = 0 \mu\text{m}$ ). Moreover, the intensity values measured in models after 10 days from HPDE-KRAS cells seeding are two-fold higher than those quantified after 7 days. Therefore, a culture period of 10 days seems to be optimal to guarantee the collimation of epithelial cells inside the cavity while maintaining a good level of proliferation.

The interactions between stromal and HPDE-KRAS cells within the cavity have been also qualitatively analyzed in confocal images at higher magnifications (Figure 7). Interestingly, the images relative to 3 and 7 days of co-culture show the tendency of epithelial cells to form 3D clusters between fibroblasts interconnections, reassembling the cell organization similar to the physiological exocrine

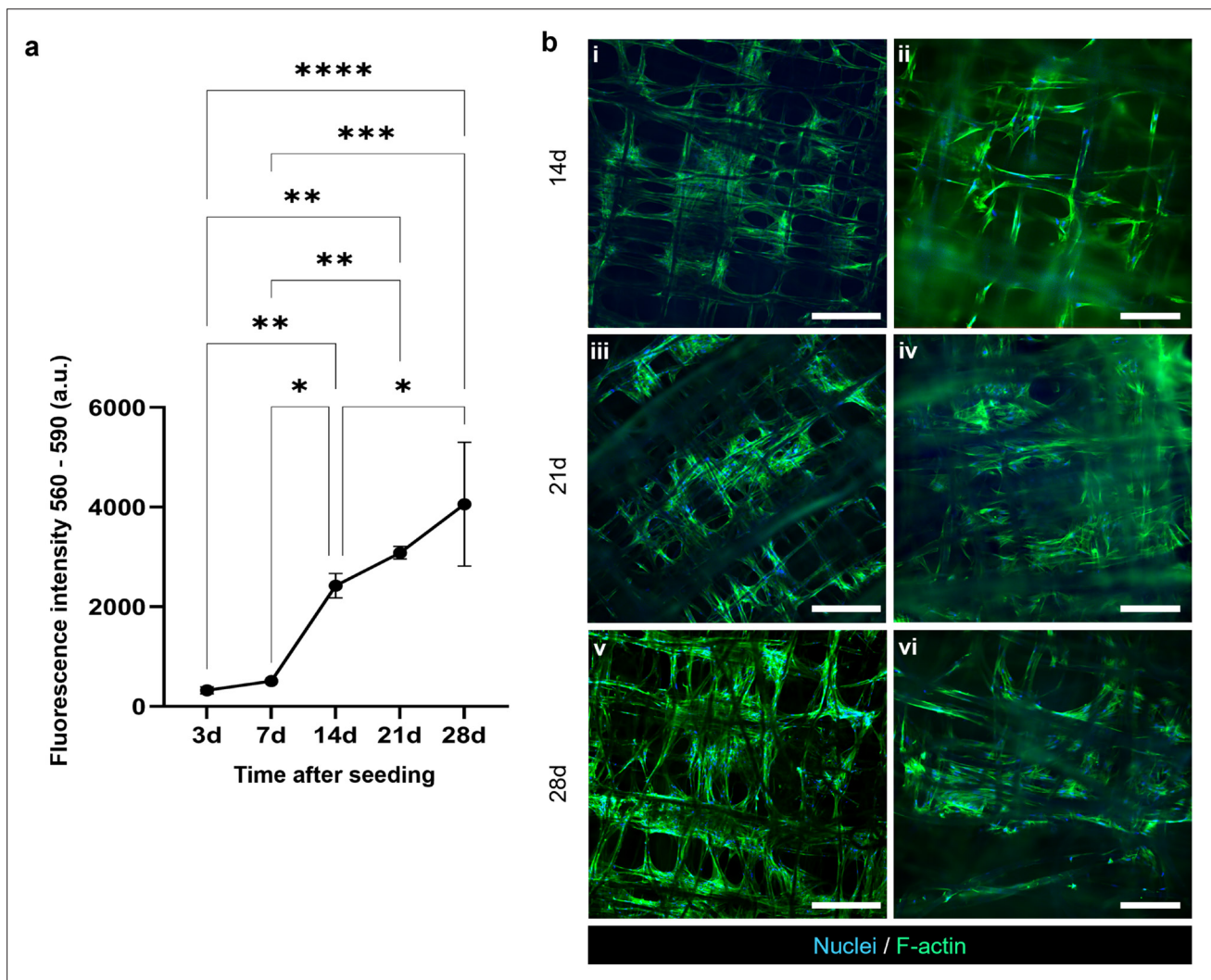


**Figure 3.** Viability and distribution of stromal cells in 3D MEW scaffolds. (a) Metabolic activity of fibroblasts seeded on MEW scaffolds as a function of time, measured from the reduction of resazurin ( $n = 3$ ). Tukey's multiple comparisons test:  $*p < 0.05$ ,  $**p < 0.01$ ,  $***p < 0.001$ ,  $****p < 0.0001$ . (b) Representative confocal images at 10× (i, iii, v) and 20× (ii, iv, vi) magnifications of HFF1 at 14, 21, and 28 days after seeding. Scale bars: 100 μm (i) and 50 μm (ii). (c) Scanning electron microscopy (SEM) images at different magnifications showing the HFF1 colonization within the MEW constructs. Scale bars: 500 μm (i, iv, vii), 100 μm (ii, v, viii), and 20 μm (iii, vi, ix).

pancreatic unit (epithelial cells surrounded by stromal cells). After 7, 10, and 14 days in co-culture, HPDE-KRAS cells visibly proliferated within the MEW model, growing on fibers and on the stromal tissue and colonizing most of the cavity's bottom.

#### 4. Discussion

Two-dimensional models are valuable low-cost systems that can be easily applied in *in vitro* experiments,<sup>45</sup> but they are unable to recapitulate the biological and biophysical complexity of human tumor microenvironment.<sup>46</sup> Indeed, several studies have largely proved that pancreatic cancer and stromal cells grown in a 3D bioengineered

environment respond to drugs differently than cells in two-dimensional models and show features more similar to the ones typical of PDAC components (e.g., chemoresistance, biochemical gradients, tumor–stroma cytoarchitecture).<sup>47–51</sup> For this reason, pancreatic cancer research has been oriented in recent years toward the development of novel *in vitro* models such as organ-on-chip and 3D models that better mimic the human tumor for *in vivo* conditions, for addressing ethical concerns in animal experiments, and to deepen our understanding of PDAC physiopathology.<sup>52,53</sup> So far, only few studies focused on replicating the 3D gland geometry of the functional unit of exocrine pancreas,<sup>23–25,54,55</sup> but they



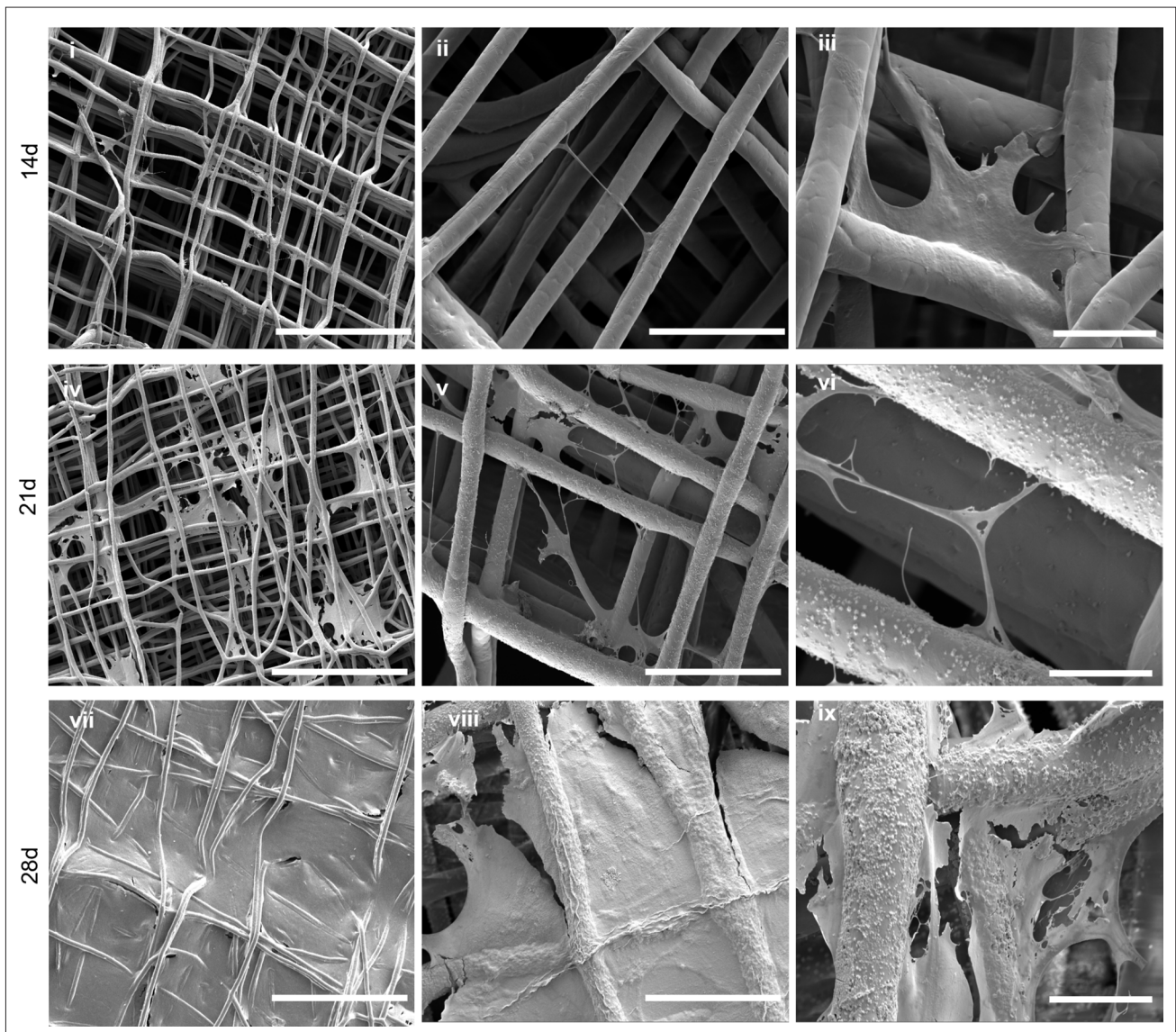


**Figure 4.** Distribution of stromal cells in 3D MEW scaffolds. Scanning electron microscopy (SEM) images at different magnifications showing the HFF1 colonization within the MEW constructs. Scale bars: 500  $\mu\text{m}$  (i, iv, vii), 100  $\mu\text{m}$  (ii, v, viii), and 20  $\mu\text{m}$  (iii, vi, ix).

failed to reproduce the acino-ductal morphology<sup>24,54</sup> or incorporate the stromal components.<sup>25,56</sup> In this work, we designed and fabricated a 3D model, a layer-by-layer PCL scaffold, that recapitulates the morphology and composition of the exocrine pancreatic functional unit. In particular, we used MEW to obtain microscale constructs, which support cells' growth and provide physiological stimuli, since the MEW fibers are similar in size to natural ECM fibers that have diameters ranging from 1 to 20  $\mu\text{m}$ <sup>57</sup> (Figure 2).

Although the accuracy in obtaining 3D complex geometries is lower in MEW compared with other layer-by-

layer techniques (e.g., fused deposition modeling), where the polymer extrusion is discontinuous and the ambient parameters (e.g., humidity and ambient temperature) poorly affect the jet stability and the filament deposition,<sup>30,58,59</sup> the work described in this paper goes beyond the state of the art in the MEW field<sup>28,31</sup> and can be considered a pioneer study creating such a complex geometry of the gland (at a millimeter scale) without the need of any supports and/or cylindrical rotary mandrels. Thus, our approach bypasses the technical difficulties in separating the printed scaffolds from the supports and permits to fabricate morphologies other than mandrels shape and dimensions.<sup>60-65</sup> It has recently been shown that complex tubular structures can



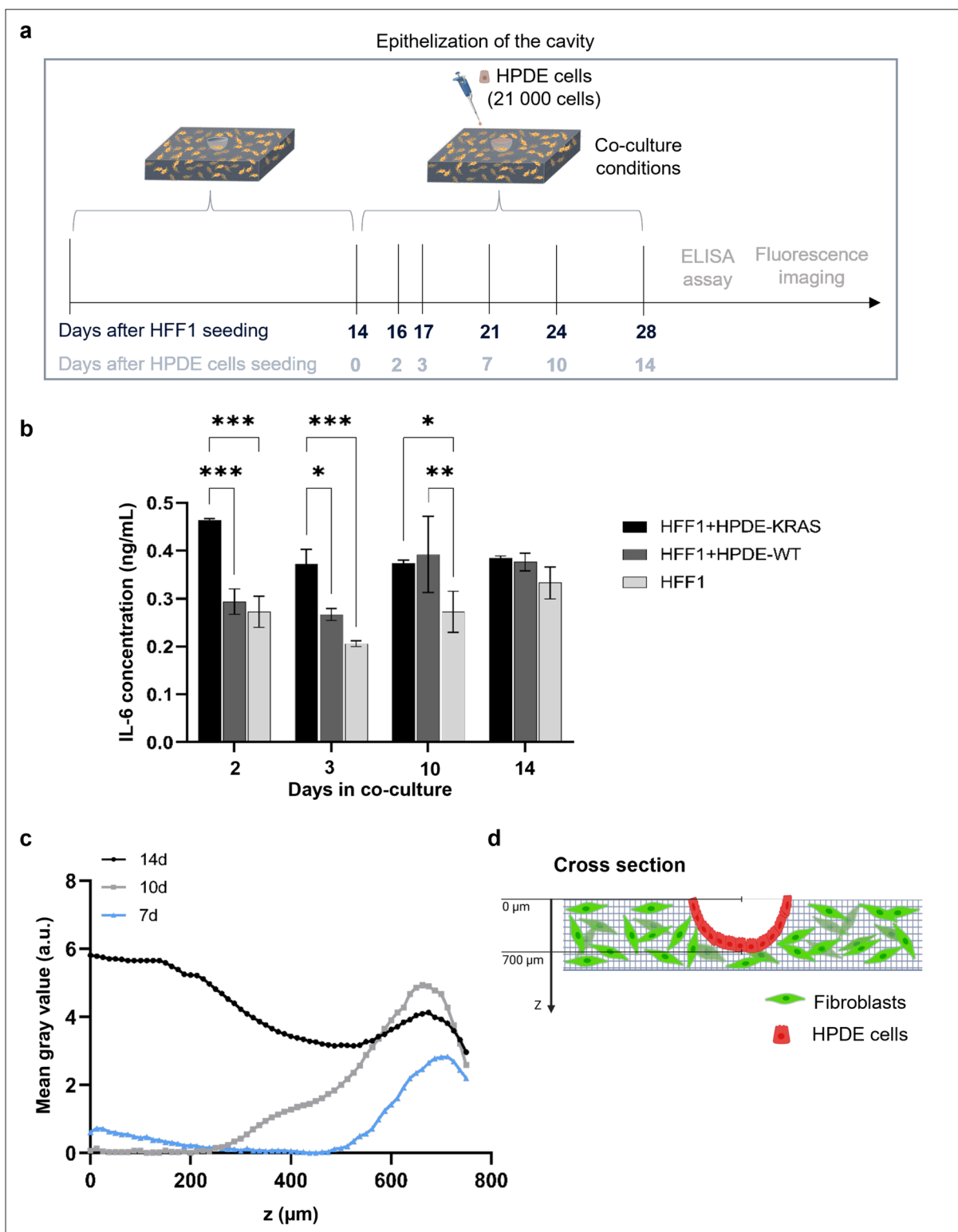


**Figure 5.** Epithelization of the cavity in the fibroblast-laden MEW scaffold. (a) Schematic illustration of the experiments pipeline. (b) Bar plots of the data obtained from ELISA test for IL-6 level for each culture condition (HFF1, HFF1 + HPDE-WT, and HFF1 + HPDE-KRAS) grouped per time step (n = 3). Each condition has been assayed in duplicate following the manufacturer’s instructions. Tukey’s multiple comparisons test: \*p < 0.05, \*\*p < 0.01, \*\*\*p < 0.001, \*\*\*\*p < 0.0001. (c) Plots reporting the intensity values of E-cadherin signal along the z-axis in constructs co-cultured with HFF1 and HPDE-KRAS cells for 7, 10, and 14 days. (d) Drawing showing the region where the z-stack images were acquired.

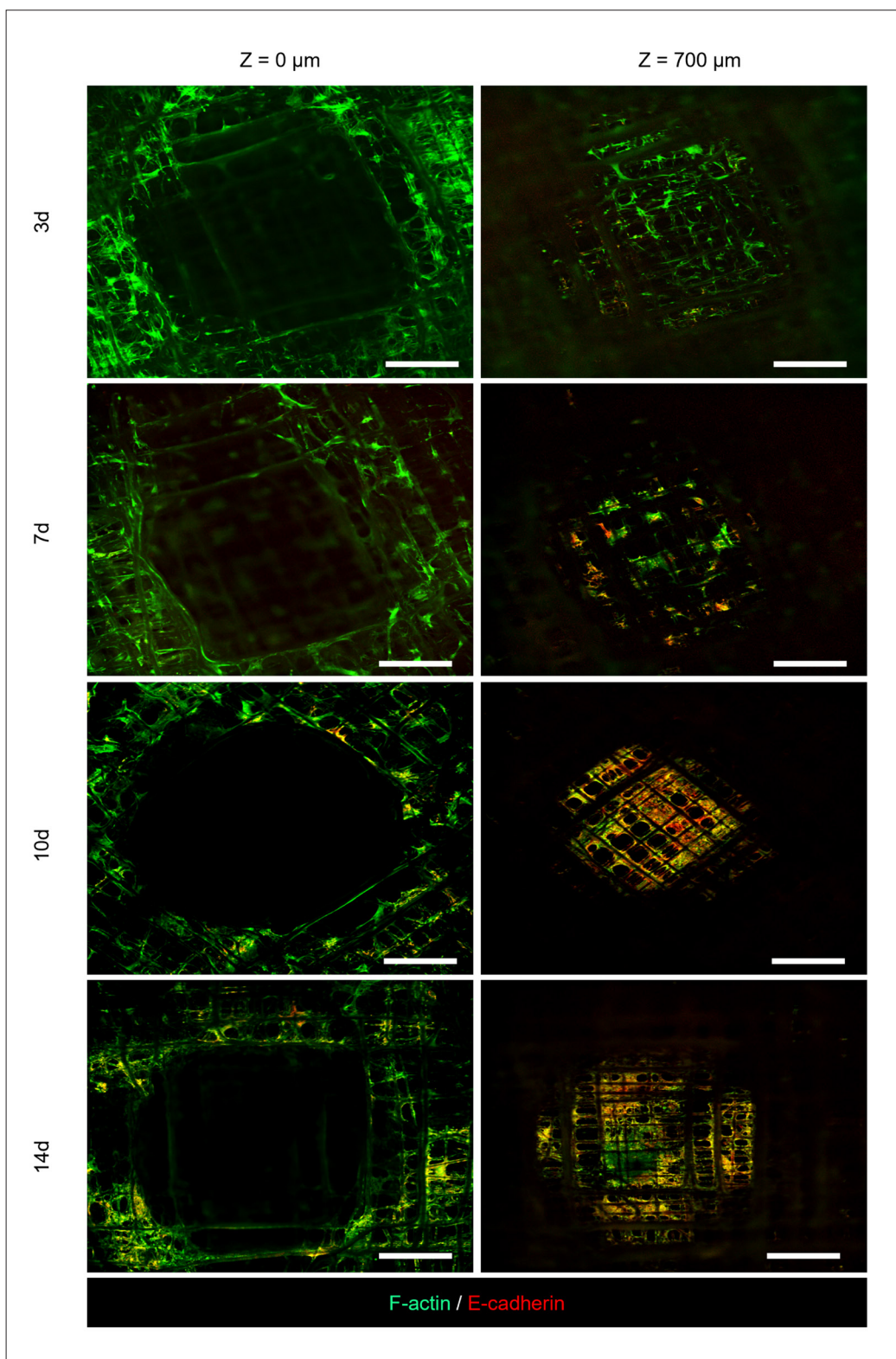


**Figure 6.** Distribution of epithelial cells co-cultured with fibroblasts in 3D MEW scaffolds. Representative confocal images at 4× magnification showing constructs slices at different depths, after 3 days, 7 days, 10 days, and 14 days from HPDE-KRAS cells seeding. Scale bars: 500 μm.

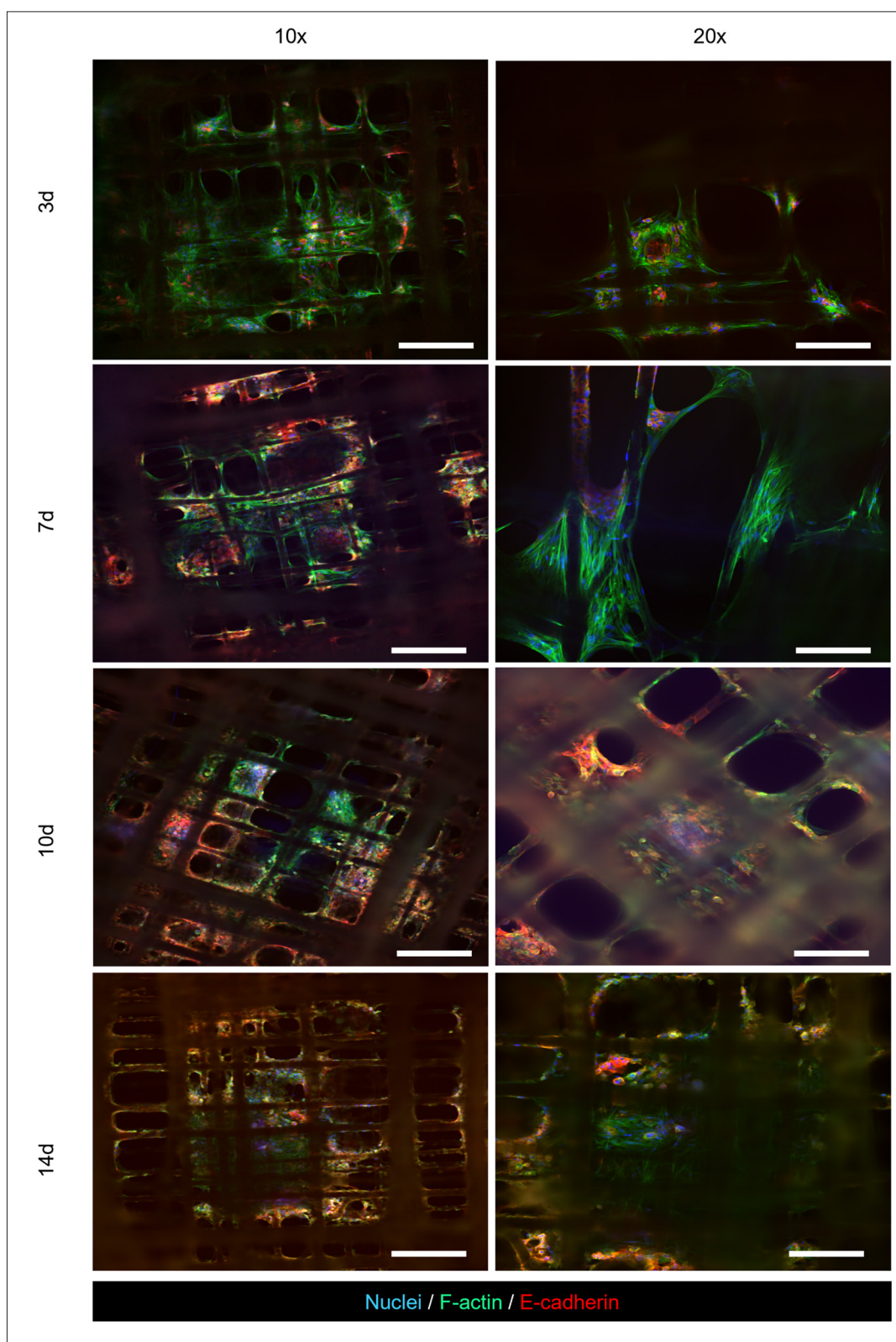


**Figure 7.** Interactions between stromal and HPDE-KRAS cells within the cavity of MEW model. Representative confocal images at 10× and 20× magnifications showing HFF1 and HPDE-KRAS cells co-cultured within the cavity, after 3 days, 7 days, 10 days, and 14 days from HPDE-KRAS cells seeding. Scale bars: 200 μm (left column) and 100 μm (right column).



be obtained by incorporating the method of layer shifting in the programmed toolpath, using planar collectors.<sup>66,67</sup> However, these scaffolds were poorly interconnected as fibers tend to adhere to each other. In contrast, we showed that the printing of complex biomimetic structures have high shape fidelity and interconnected porosity, which are key features for biological studies as confirmed by adhesion and proliferation assays using stromal cells (HFF1) that remained viable and active for at least 4 weeks in MEW constructs (Figure 3). These results are supported by other studies in literature, showing the culture of cells on PCL scaffolds obtained by MEW for several weeks.<sup>61,68</sup> Therefore, our results confirm the ability of these biomimetic scaffolds in promoting cell growth and tissue formation, in line with the numerous studies reporting the large use of PCL in additive manufacturing approaches for biomedical applications.<sup>37-40</sup>

The model developed in this study was able to maintain long-term culture of human fibroblasts, which adhered to different fibers to create bridges across the pores and grew with the support of polymeric grid, imitating the natural process. The surface of MEW scaffolds was almost covered by a thin layer of stromal matrix after 28 days in culture (Figure 4).

Moreover, we detected the presence of granular corpuscles on fibers of MEW models, at 21 days and 28 days after HFF1 seeding. Evidence in literature seems to confirm our hypothesis that correlates the presence of such corpuscles with the deposition of ECM by fibroblasts.<sup>69,70</sup> However, further analyses are needed to confirm this statement.

Human pancreatic ductal epithelial cells were seeded in the cavity of the structures, where HFF1 were allowed to grow for 2 weeks (Figure 5). The epithelial–stromal cells crosstalk occurring in the MEW model was studied in terms of fibroblasts inflammation mediated by IL-6 (Figure 5b). Indeed, the release of IL-6 by inflamed tumor-associated fibroblasts plays a key role in PDAC–stroma interplay and regulates a wide range of mechanisms involved in pancreatic cancer, such as angiogenesis, epithelial-to-mesenchymal transition, and immunosuppression.<sup>71-73</sup> It has been demonstrated previously that the release of IL-6 by HPDE-KRAS cells under monoculture on artificial substrates was minimal and negligible compared to HFF1.<sup>21</sup> Our results indicate a higher IL-6 release by fibroblasts in co-culture with HPDE-KRAS cells for 2 days and 3 days, in comparison with HFF1 alone or HFF1 under co-culture with healthy HPDE cells (HPDE-WT). This is in line with studies in literature reporting the role of the *KRAS* oncogene as a driver for the IL-6 production by stromal cells.<sup>74,75</sup>

The MEW model developed in this study recapitulates the *in vivo* pathological condition, accompanied by IL-6 secretion by fibroblasts during the inflammation of

cancer cells.<sup>76</sup> The ability of this model in reproducing the inflammatory cascade occurring in pancreatic cancer is further confirmed by numerous studies showing notable differences in serum IL-6 levels between PDAC patients and healthy individuals.<sup>77-83</sup>

However, the differences in IL-6 levels of fibroblasts co-cultured with either healthy epithelial cells or epithelial cells overexpressing *KRAS* were statistically significant only at early stages of the experiment, suggesting that the IL-6-mediated inflammation occurred mainly during the first few hours (up to 72 h). At later phases of the experiment, inflammation might be mediated by other proteins.<sup>84</sup>

The ability of the human MEW model in reproducing the natural compartmentalization typical of the exocrine pancreatic microenvironment was demonstrated, as the epithelial cells were localized within the cavity while fibroblasts colonized the 3D structure. Indeed, HPDE-KRAS cells colonized the acino-like structure and remained collimated in the cavity up to 10 days of co-culture period and then started to migrate within the scaffold and on the scaffold upper surface (Figure 5c and d, and Figure 6; and Videos S1–S3 in Supplementary File). Therefore, the optimal protocol for co-culture implementation within the MEW structure was set: 14 days of fibroblasts culture alone plus 10 days of fibroblasts and epithelial cells co-culture. Indeed, these time points permit the creation of a cellularized MEW model that mimics the native compartmentalized 3D tumor architecture, which is widely recognized to significantly influence behavior of cancer cells.<sup>22,85,86</sup> Moreover, the crosstalk between stromal and epithelial cells can also be easily monitored in this model, as the open structure allows the observation of the epithelial cell organization within the cavity, between the fibroblast interconnections (Figure 7). Although these results demonstrate the possibility to model the functional unit of the exocrine pancreas *in vitro* and to study the interactions between PDAC and stromal cells occurring at different stages of pancreatic cancer progression in a very controlled and biomimetic way, additional works are warranted to improve this model. For instance, advanced bioprinting systems can be employed in combination with MEW<sup>87</sup> to print the epithelial cells into a monolayer on the previously obtained MEW model, within the acinar-like cavity in a precise and software-guided way.

## 5. Conclusion

This work describes the engineering approach adopted to fabricate a layer-by-layer microscale model resembling the half structure of the functional unit of the exocrine pancreas, for the study of pancreatic cancer. MEW was employed to obtain the complex 3D structure without the

need for supports, mandrels, or sacrificial materials. The constructed PCL scaffold represents, at the microscale, a biomimetic porous network able to support the growth and proliferation of stromal cells over several weeks. In particular, human fibroblasts and HPDE overexpressing the *KRAS* oncogene were used to replicate the stromal and cancer epithelial components, respectively. The ability of this model in promoting the formation of a stromal tissue after 28 days of culture, as well as the capability in replicating the compartmentalized architecture typical of the pancreatic cancer microenvironment by hosting both stromal cells and epithelial cells, was assessed. Indeed, the specific localization of the epithelial cells within the acinar cavity was achieved and maintained up to 10 days. Moreover, the MEW model features the crosstalk between stromal and PDAC cells on IL-6 release, mirroring the pathological condition *in vivo*.

Therefore, the successful realization of the biomimetic construct described in this paper provides an important step toward a fully human 3D *in vitro* model of the pancreatic gland capable of recapitulating acinar morphology, allowing long-term analyses of pancreatic cancer progression from the very early stages and facilitating the design of effective treatments against this cancer.

## Acknowledgments

We thank Prof. F. Bussolino for the support in cell culturing.

## Funding

This project was carried out with the support of Fondazione Compagnia di San Paolo - Trapezio Call for Proposals -Target 1 project “ExocRine glandular Tissue mOdels TExocRine glandular Tissue mOdels Through precisely designed biomimetic EnviroNmEnts: an engineering tools to improve understanding and treatment for pancreatic cancer (ERATOSTHENES)”.

## Conflict of interest

The authors declare no conflicts of interest.

## Author Contributions

*Conceptualization:* Gianluca Ciardelli, Chiara Tonda-Turo

*Data curation:* Viola Sgarminato, Michela Licciardello

*Formal analysis:* Viola Sgarminato, Chiara Tonda-Turo

*Funding acquisition:* Gianluca Ciardelli, Chiara Tonda-Turo

*Investigation:* Viola Sgarminato, Michela Licciardello, Chiara Tonda-Turo

*Methodology:* Michela Licciardello, Chiara Tonda-Turo

*Writing – original draft:* Viola Sgarminato, Chiara Tonda-Turo

*Writing – review & editing:* Gianluca Ciardelli

## Ethics approval and consent to participate

Not applicable.

## Consent for publication

Not applicable.

## Availability of data

Data are available from the corresponding author upon reasonable request.

## References

- Hegyí P, Petersen OH. The exocrine pancreas: the acinar-ductal tango in physiology and pathophysiology. *Rev Physiol Biochem Pharmacol.* 2013;165:1-30. doi: 10.1007/112\_2013\_14
- Shih HP, Wang A, Sander M. Pancreas organogenesis: from lineage determination to morphogenesis. *Annu Rev Cell Dev Biol.* 2013;29:81-105. doi: 10.1146/annurev-cellbio-101512-122405
- Weniger M, Honselmann KC, Liss AS. The extracellular matrix and pancreatic cancer: a complex relationship. *Cancers.* 2018;10(9):316. doi: 10.3390/cancers10090316
- Fu Y, Liu S, Zeng S, Shen H. The critical roles of activated stellate cells-mediated paracrine signaling, metabolism and onco-immunology in pancreatic ductal adenocarcinoma. *Mol Cancer.* 2018;17:62. doi: 10.1186/s12943-018-0815-z
- Pothula SP, Pirola RC, Wilson JS, Apte MV. Pancreatic stellate cells: aiding and abetting pancreatic cancer progression. *Pancreatol.* 2020;20:409-418. doi: 10.1016/j.pan.2020.01.003
- Wang S, Li Y, Xing C, et al. Tumor microenvironment in chemoresistance, metastasis and immunotherapy of pancreatic cancer. *Am J Cancer Res.* 2020;10:1937-1953.
- Bynigeri RR, Jakkampudi A, Jangala R, et al. Pancreatic stellate cell: Pandora's box for pancreatic disease biology. *World J Gastroenterol.* 2017;23:382. doi: 10.3748/wjg.v23.i3.382
- Apte MV, Wilson JS, Lugea A, Pandol SJ. A starring role for stellate cells in the pancreatic cancer microenvironment. *Gastroenterology.* 2013;144:1210-1219. doi: 10.1053/j.gastro.2012.11.037
- Wu Y, Zhang C, Jiang K, Werner J, Bazhin AV, D'Haese JG. The role of stellate cells in pancreatic ductal adenocarcinoma: targeting perspectives. *Front Oncol.* 2021;10. doi: 10.3389/fonc.2020.621937
- Zhan HX, Zhou B, Cheng Y, et al. Crosstalk between stromal cells and cancer cells in pancreatic cancer: new insights into stromal biology. *Cancer Lett.* 2017;392:83-93. doi: 10.1016/j.canlet.2017.01.041

11. Cui SJ, Tang TY, Zou XW, Su Q-M, Feng L, Gong X-Y. Role of imaging biomarkers for prognostic prediction in patients with pancreatic ductal adenocarcinoma. *Clin Radiol.* 2020;75:478.e1-478.e11. doi: 10.1016/j.crad.2019.12.023
12. Orth M, Metzger P, Gerum S, et al. Pancreatic ductal adenocarcinoma: Biological hallmarks, current status, and future perspectives of combined modality treatment approaches. *Radiat Oncol.* 2019;14(1):141. doi: 10.1186/s13014-019-1345-6
13. Porciuncula A, Hajdu C, David G. The dual role of senescence in pancreatic ductal adenocarcinoma. *Adv Cancer Res.* 2016;131:1-20. doi: 10.1016/bs.acr.2016.05.006
14. Brunet LR, Hagemann T, Andrew G, Mudan S, Marabelle A. Have lessons from past failures brought us closer to the success of immunotherapy in metastatic pancreatic cancer? *Oncoimmunology.* 2016;5(4). doi: 10.1080/2162402X.2015.1112942
15. Cave DD, Rizzo R, Sainz B, Gigli G, Del Mercato LL, Lonardo E. The revolutionary roads to study cell-cell interactions in 3d in vitro pancreatic cancer models. *Cancers (Basel).* 2021;13(4):930. doi: 10.3390/cancers13040930
16. Osuna de la Peña D, Trabulo S, Collin E, et al. Bioengineered 3D models of human pancreatic cancer recapitulate in vivo tumour biology. *Nat Commun.* 2021;12:5623. doi: 10.1038/s41467-021-25921-9
17. Haque MR, Rempert TH, Al-Hilal TA, Wang C, Bhushan A, Bishehsari F. Organ-chip models: opportunities for precision medicine in pancreatic cancer. *Cancers (Basel).* 2021;13(17):4487. doi: 10.3390/cancers13174487
18. Mollica H, Teo YJ, Tan DZ, et al. A 3D pancreatic tumor model to study T cell infiltration. *Biomater Sci.* 2021;9:7420-7431. doi: 10.1039/D1BM00210D
19. Schuster B, Junkin M, Kashaf SS, et al. Automated microfluidic platform for dynamic and combinatorial drug screening of tumor organoids. *Nat Commun.* 2020;11:1-12. doi: 10.1038/s41467-020-19058-4
20. Nguyen, DHT, Lee E, Alimperti S, et al. A biomimetic pancreatic cancer on-chip reveals endothelial ablation via ALK7 signaling. *Sci Adv.* 2019;5(8):eaav6789. doi: 10.1126/sciadv.aav6789
21. Sgarminato V, Marasso SL, Cocuzza M, et al. PDAC-on-chip for in vitro modeling of stromal and pancreatic cancer cell crosstalk. *Biomater Sci.* 2022;11:208-224. doi: 10.1039/D2BM00881E
22. Kota J, Hancock J, Kwon J, Korc M. Pancreatic cancer: stroma and its current and emerging targeted therapies. *Cancer Lett.* 2017;391:38-49. doi: 10.1016/j.canlet.2016.12.035
23. Hajiabbas M, D'Agostino C, Simińska-Stanny J, Tran SD, Shavandi A, Delporte C. Bioengineering in salivary gland regeneration. *J Biomed Sci.* 2022;291(29):1-24. doi: 10.1186/s12929-022-00819-w
24. Gupta P, Pérez-Mancera PA, Kocher H, Nisbet A, Schettino G, Velliou EG. A novel scaffold-based hybrid multicellular model for pancreatic ductal adenocarcinoma—toward a better mimicry of the in vivo tumor microenvironment. *Front Bioeng Biotechnol.* 2020;8:290. doi: 10.3389/fbioe.2020.00290
25. Venis SM, Moon HR, Yang Y, Utturkar SM, Konieczny SF, Han B. Engineering of a functional pancreatic acinus with reprogrammed cancer cells by induced: PTF1a expression. *Lab Chip.* 2021;21:3675-3685. doi: 10.1039/d1lc00350j
26. Charbonneau AM, Kinsella JM, Tran SD. 3D cultures of salivary gland cells in native or gelled egg yolk plasma, combined with egg white and 3D-printing of gelled egg yolk plasma. *Materials (Basel).* 2019;12(21):3480. doi: 10.3390/ma12213480
27. Jain P, Kathuria H, Dubey N. Advances in 3D bioprinting of tissues/organs for regenerative medicine and in-vitro models. *Biomaterials.* 2022;287:121639. doi: 10.1016/j.biomaterials.2022.121639
28. Loewner S, Heene S, Baroth T, et al. Recent advances in melt electro writing for tissue engineering for 3D printing of microporous scaffolds for tissue engineering. *Front Bioeng Biotechnol.* 2022;10. doi: 10.3389/fbioe.2022.896719
29. Hutmacher DW, Dalton PD. Melt electrospinning. *Chem Asian J.* 2011;6:44-56. doi: 10.1002/asia.201000436
30. Kade JC, Dalton PD. Polymers for melt electrowriting. *Adv Healthc Mater.* 2021;10(1):2001232. doi: 10.1002/adhm.202001232
31. Cao K, Zhang F, Zaeri A, et al. Advances in design and quality of melt electrowritten scaffolds. *Mater Des.* 2023;1:226. doi: 10.1016/j.matdes.2023.111618
32. Moroni L, Boland T, Burdick JA, et al. Biofabrication: a guide to technology and terminology. *Trends Biotechnol.* 2018;36:384-402. doi: 10.1016/j.tibtech.2017.10.015
33. Fu Z, Naghieh S, Xu C, Wang C, Sun W, Chen X. Printability in extrusion bioprinting. *Biofabrication.* 2021;13(3):033001. doi: 10.1088/1758-5090/abe7ab
34. Licciardello M, Ciardelli G, Tonda-Turo C. Biocompatible electrospun polycaprolactone-polyaniline scaffold treated with atmospheric plasma to improve hydrophilicity. *Bioengineering.* 2021;8(2):24. doi: 10.3390/bioengineering8020024



35. Mancuso E, Tonda-Turo C, Ceresa C, et al. Potential of Manuka honey as a natural polyelectrolyte to develop biomimetic nanostructured meshes with antimicrobial properties. *Front Bioeng Biotechnol.* 2019;7:344. doi: 10.3389/fbioe.2019.00344
36. Giuntoli G, Muzio G, Actis C, et al. In-vitro characterization of a hernia mesh featuring a nanostructured coating. *Front Bioeng Biotechnol.* 2021;8:589223. doi: 10.3389/fbioe.2020.589223
37. Backes, EH, Harb SV, Beatrice CA, et al. Polycaprolactone usage in additive manufacturing strategies for tissue engineering applications: a review. *J Biomed Mater Res B Appl Biomater.* 2022;110:1479-1503. doi: 10.1002/jbm.b.34997
38. Großhaus C, Bakirci E, Berthel M, et al. Melt electrospinning of nanofibers from medical-grade poly( $\epsilon$ -caprolactone) with a modified nozzle. *Small.* 2020;16:2003471. doi: 10.1002/sml.202003471
39. Kumar N, Joisher H, Ganguly A. Polymeric scaffolds for pancreatic tissue engineering: a review. *Rev Diabet Stud.* 2017;14:334-353. doi: 10.1900/RDS.2017.14.334
40. Yang X, Wang Y, Zhou Y, Chen J, Wan Q. The application of polycaprolactone in three-dimensional printing scaffolds for bone tissue engineering. *Polymers (Basel).* 2021;13:2754. doi: 10.3390/polym13162754
41. Abràmoff MD, Magalhães PJ, Ram SJ. Image processing with ImageJ. *Biophotonics Int.* 2004;11:36-42.
42. Lee JH, Kim SK, Khawar IA, Jeong S-Y, Chung S, Kuh H-J. Microfluidic co-culture of pancreatic tumor spheroids with stellate cells as a novel 3D model for investigation of stroma-mediated cell motility and drug resistance. *J Exp Clin Cancer Res.* 2018;37:1-12. doi: 10.1186/s13046-017-0654-6
43. Jeong SY, Lee JH, Shin Y, Chung S, Kuh H-J. Co-culture of tumor spheroids and fibroblasts in a collagen matrix-incorporated microfluidic chip mimics reciprocal activation in solid tumor microenvironment. *PLoS One.* 2016;11:e0159013. doi: 10.1371/journal.pone.0159013
44. Fujiwara M, Kanayama K, Hirokawa YS, Shiraishi T. ASF-4-1 fibroblast-rich culture increases chemoresistance and mTOR expression of pancreatic cancer BxPC-3 cells at the invasive front in vitro, and promotes tumor growth and invasion in vivo. *Oncol Lett.* 2016;11:2773. doi: 10.3892/ol.2016.4289
45. Weeber F, Ooft SN, Dijkstra KK, Voest EE. Tumor organoids as a pre-clinical cancer model for drug discovery. *Cell Chem Biol.* 2017;24:1092-1100. doi: 10.1016/j.chembiol.2017.06.012
46. Kapałczyńska M, Kolenda T, Przybyła W, et al. 2D and 3D cell cultures - a comparison of different types of cancer cell cultures. *Arch Med Sci.* 2018;14:910-919. doi: 10.5114/aoms.2016.63743
47. Desoize B, Jardillier J. Multicellular resistance: a paradigm for clinical resistance? *Crit Rev Oncol Hematol.* 2000;36:193-207. doi: 10.1016/s1040-8428(00)00086-x
48. Brancato V, Oliveira JM, Correló VM, Reis RL, Kundu SC. Could 3D models of cancer enhance drug screening? *Biomaterials.* 2020;232:119744. doi: 10.1016/j.biomaterials.2019.119744
49. Shichi Y, Norihiko S, Masaki M, et al. Enhanced morphological and functional differences of pancreatic cancer with epithelial or mesenchymal characteristics in 3D culture. *Sci Rep.* 2019;9:10871. doi: 10.1038/s41598-019-47416-w
50. Fang Y, Eglen RM. Three-dimensional cell cultures in drug discovery and development. *SLAS Discov.* 2017;22:456-472. doi: 10.1177/1087057117696795
51. Laschke MW, Menger MD. Life is 3D: boosting spheroid function for tissue engineering. *Trends Biotechnol.* 2017;35:133-144. doi: 10.1016/j.tibtech.2016.08.004
52. Tomás-Bort E, Kieler M, Sharma S, Candido JB, Loessner D. 3D approaches to model the tumor microenvironment of pancreatic cancer. *Theranostics.* 2020;10:5074-5089. doi: 10.7150/thno.42441
53. Monteiro MV, Ferreira LP, Rocha M, Gaspar VM, Mano JF. Advances in bioengineering pancreatic tumor-stroma physiometric biomodels. *Biomaterials.* 2022;287:121653. doi: 10.1016/j.biomaterials.2022.121653
54. Bradney MJ, Venis SM, Yang Y, Konieczny SF, Han B. A biomimetic tumor model of heterogeneous invasion in pancreatic ductal adenocarcinoma. *Small.* 2020;16(10):e1905500. doi: 10.1002/sml.201905500
55. Sung JH, Shuler ML. Microtechnology for mimicking in vivo tissue environment. *Ann Biomed Eng.* 2012;40:1289-1300. doi: 10.1007/s10439-011-0491-2
56. Randriamanantsoa S, Papargyriou A, Maurer HC, et al. Spatiotemporal dynamics of self-organized branching in pancreas-derived organoids. *Nat Commun.* 2022;13:1-15. doi: 10.1038/s41467-022-32806-y
57. Ushiki T. Collagen fibers, reticular fibers and elastic fibers. A comprehensive understanding from a morphological viewpoint. *Arch Histol Cytol.* 2002;65:109-126. doi: 10.1679/aohc.65.109
58. Rajan K, Samykano M, Kadirgama K, Harun WSW, Rahman MM. Fused deposition modeling: process, materials, parameters, properties, and applications. *Int J Adv Manuf Technol.* 2022;120:1531-1570. doi: 10.1007/s00170-022-08860-7
59. Bachs-Herrera A, Yousefzade O, Del Valle LJ, Puiggali J. Melt electrospinning of polymers: blends, nanocomposites, additives and applications. *Appl Sci.* 2021;11(4):1808. doi: 10.3390/app11041808

60. Saily NT, Shabab T, Bas O, et al. Melt electrowriting of complex 3D anatomically relevant scaffolds. *Front Bioeng Biotechnol.* 2020;8:793. doi: 10.3389/fbioe.2020.00793
61. Peiffer QC, de Ruijter M, van Duijn J, et al. Melt electrowriting onto anatomically relevant biodegradable substrates: resurfacing a diarthrodial joint. *Mater Des.* 2020;195:109025. doi: 10.1016/j.matdes.2020.109025
62. Brooks-Richards TL, Paxton NC, Allenby MC, Woodruff MA. Dissolvable 3D printed PVA moulds for melt electrowriting tubular scaffolds with patient-specific geometry. *Mater Des.* 2022;215:110466. doi: 10.1016/j.matdes.2022.110466
63. Saha U, Nairn R, Keenan O, Monaghan MG. A deeper insight into the influence of the electric field strength when melt-electrowriting on non-planar surfaces. *Macromol Mater Eng.* 2021;306:2100496. doi: 10.1002/mame.202100496
64. Constante G, Apsite I, Alkhamis H, et al. 4D biofabrication using a combination of 3D printing and melt-electrowriting of shape-morphing polymers. *ACS Appl Mater Interfaces.* 2021;13:12767-12776. doi: 10.1021/acsami.0c18608
65. Van Genderen AM, Jansen K, Kristen M, et al. Topographic guidance in melt-electrowritten tubular scaffolds enhances engineered kidney tubule performance. *Front Bioeng Biotechnol.* 2021;8:617364. doi: 10.3389/fbioe.2020.617364
66. Liashenko I, Hrynevich A, Dalton PD. Designing outside the box: unlocking the geometric freedom of melt electrowriting using microscale layer shifting. *Adv Mater.* 2020;32:2001874. doi: 10.1002/adma.202001874
67. Bakirci E, Schaefer N, Dahri O, et al. Melt electrowritten in vitro radial device to study cell growth and migration. *Adv Biosyst.* 2020;4:2000077. doi: 10.1002/adbi.202000077
68. Korpershoek JV, Korpershoek JV, Ruijter M, et al. Potential of melt electrowritten scaffolds seeded with meniscus cells and mesenchymal stromal cells. *Int J Mol Sci.* 2021;22:11200. doi: 10.3390/ijms222011200
69. Neves SC, Moreira Teixeira LS, Moroni L, et al. Chitosan/poly( $\epsilon$ -caprolactone) blend scaffolds for cartilage repair. *Biomaterials.* 2011;32:1068-1079. doi: 10.1016/j.biomaterials.2010.09.073
70. Malakpour Permlid A, Roci P, Fredlund E, et al. Unique animal friendly 3D culturing of human cancer and normal cells. *Toxicol In Vitro.* 2019;60:51-60. doi: 10.1016/j.tiv.2019.04.022
71. Kuen J, Darowski D, Kluge T, Majety M. Pancreatic cancer cell/fibroblast co-culture induces M2 like macrophages that influence therapeutic response in a 3D model. *PLoS One.* 2017;12:e0182039. doi: 10.1371/journal.pone.0182039
72. van Duijneveldt G, Griffin MDW, Putoczki TL. Emerging roles for the IL-6 family of cytokines in pancreatic cancer. *Clin Sci.* 2020;134:2091-2115. doi: 10.1042/CS20191211
73. Öhlund D, Handly-Santana A, Biffi G, et al. Distinct populations of inflammatory fibroblasts and myofibroblasts in pancreatic cancer. *J Exp Med.* 2017;214:579-596. doi: 10.1084/jem.20162024
74. Feurino LW, Zhang Y, Bharadwaj U, et al. IL-6 stimulates Th2 type cytokine secretion and upregulates VEGF and NRP-1 expression in pancreatic cancer cells. *Cancer Biol Ther.* 2007;6:1096-1100. doi: 10.4161/cbt.6.7.4328
75. Ancrile B, Lim KH, Counter CM. Oncogenic Ras-induced secretion of IL6 is required for tumorigenesis. *Genes Dev.* 2007;21:1714-1719. doi: 10.1101/gad.1549407
76. Nagasaki T, Hara M, Nakanishi H, Takahashi H, Sato M, Takeyama H. Interleukin-6 released by colon cancer-associated fibroblasts is critical for tumour angiogenesis: anti-interleukin-6 receptor antibody suppressed angiogenesis and inhibited tumour-stroma interaction. *Br J Cancer.* 2014;110:469-478. doi: 10.1038/bjc.2013.748
77. Ebrahimi B, Tucker SL, Li D, Abbruzzese JL, Kurzrock R. Cytokines in pancreatic carcinoma. *Cancer.* 2004;101:2727-2736. doi: 10.1002/cncr.20672
78. Wigmore SJ, Fearon KC, Sangster K, Maingay JP, Garden OJ, Ross JA. Cytokine regulation of constitutive production of interleukin-8 and -6 by human pancreatic cancer cell lines and serum cytokine concentrations in patients with pancreatic cancer. *Int J Oncol.* 2002;21:881-886. doi: 10.3892/ijo.21.4.881
79. Talar-Wojnarowska R, Gasiorowska A, Smolarz B, Romanowicz-Makowska H, Kulig A, Malecka-Panas E. Clinical significance of interleukin-6 (IL-6) gene polymorphism and IL-6 serum level in pancreatic adenocarcinoma and chronic pancreatitis. *Dig Dis Sci.* 2009;54:683-689. doi: 10.1007/s10620-008-0390-z
80. Barber MD, Fearon KCH, Ross JA. Relationship of serum levels of interleukin-6, soluble interleukin-6 receptor and tumour necrosis factor receptors to the acute-phase protein response in advanced pancreatic cancer. *Clin Sci.* 1999;96:83-87.
81. Okada S, Okusaka T, Ishii H, et al. Elevated serum interleukin-6 levels in patients with pancreatic cancer. *Jpn J Clin Oncol.* 1998;28:12-15. doi: 10.1093/jjco/28.1.12

82. Błogowski W, Deskur A, Budkowska M, et al. Selected cytokines in patients with pancreatic cancer: a preliminary report. *PLoS One*. 2014;9:e97613.  
doi: 10.1371/journal.pone.0097613
83. Mroczko B, Groblewska M, Gryko M, Kędra B, Szmitkowski M. Diagnostic usefulness of serum interleukin 6 (IL-6) and C-reactive protein (CRP) in the differentiation between pancreatic cancer and chronic pancreatitis. *J Clin Lab Anal*. 2010;24:256-261.  
doi: 10.1002/jcla.20395
84. Chen K, Wang Q, Li M, et al. Single-cell RNA-seq reveals dynamic change in tumor microenvironment during pancreatic ductal adenocarcinoma malignant progression. *EBioMedicine*. 2021;66:103315.  
doi: 10.1016/j.ebiom.2021.103315
85. Pothula SP, Pirola RC, Wilson JS, Apte MV. Pancreatic stellate cells: aiding and abetting pancreatic cancer progression. *Pancreatology*. 2020;20:409-418.  
doi: 10.1016/j.pan.2020.01.003
86. Koikawa K, Ohuchida K, Ando Y, et al. Basement membrane destruction by pancreatic stellate cells leads to local invasion in pancreatic ductal adenocarcinoma. *Cancer Lett*. 2018;425:65-77.  
doi: 10.1016/j.canlet.2018.03.031
87. Dufour A, Gallostra XB, O'Keeffe C, et al. Integrating melt electrowriting and inkjet bioprinting for engineering structurally organized articular cartilage. *Biomaterials*. 2022;283:121405.  
doi: 10.1016/j.biomaterials.2022.121405